Title

Cation and anion topotactic transformations in cobaltite thin films leading to Ruddlesden-Popper phases

Journal

Physical Review Materials, 5(6)

ISSN

2476-0455

Authors

Chiu, I-Ting
Lee, Min-Han
Cheng, Shaobo
et al.

Publication Date

2021-06-01

DOI

10.1103/physrevmaterials.5.064416

Cation and Anion Topotactic Transformations in Cobaltite Thin Films Leading to Ruddlesden-Popper Phases

I-Ting Chiu[1], Min-Han Lee[2,3], Shaobo Cheng[4], Shenli Zhang[5], Larry Heki[6], Zhen Zhang[7], Yahya Mohtashami[8], Pavel N. Lapa[3], Mingzhen Feng[9], Padraic Shafer[10], Alpha T. N'Diaye[10], Apurva Mehta[11], Jon A. Schuller[8], Giulia Galli[5,12], Shriram Ramanathan[7], Yimei Zhu[4], Ivan K. Schuller[2,3], and Yayoi Takamura[9]

[1] Department of Chemical Engineering, University of California, Davis, Davis, CA 95616

[2] Materials Science and Engineering Program, University of California, San Diego, La Jolla, CA 92093

[3] Department of Physics and Center for Advanced Nanoscience, University of California, San Diego, La Jolla, CA 92093

[4] Condensed Matter Physics and Materials Science Division, Brookhaven National Laboratory, Upton, NY, 11973

[5] Pritzker School of Molecular Engineering, The University of Chicago, Chicago, IL 60637

[6] Department of Material Science and Engineering, University of California, Santa Barbara, Santa Barbara, CA 93106

[7] School of Materials Engineering, Purdue University, West Lafayette, IN 47907

[8] Department of Electrical and Computer Engineering, University of California, Santa Barbara, Santa Barbara, CA 93106

[9] Department of Materials Science and Engineering, University of California, Davis, Davis, CA 95616

[10] Advanced Light Source, Lawrence Berkeley National Laboratory, Berkeley, CA 94720

[11] Stanford Synchrotron Radiation Lightsource, SLAC National Accelerator Laboratory, Menlo Park, CA 94025

[12] Materials Science Division and Center for Molecular Engineering, Argonne National Laboratory, Lemont, IL 60439

Keywords

Topotactic transformations, Ruddlesden-Popper, Cobaltite thin films, Magnetic oxides

Abstract

Topotactic transformations involve structural changes between related crystal structures due to a loss or gain of material while retaining a crystallographic relationship.

The perovskite oxide $La_{0.7}Sr_{0.3}CoO_3$ (LSCO) is an ideal system for investigating phase transformations due to its high oxygen vacancy conductivity, relatively low oxygen vacancy formation energy, and strong coupling of the magnetic and electronic properties to the oxygen stoichiometry. While the transition between cobaltite perovskite and brownmillerite (BM) phases has been widely reported, further reduction beyond the BM phase lacks systematic studies. In this work, we study the evolution of the physical properties of LSCO thin films upon exposure to highly reducing environments. We observe the rarely-reported crystalline Ruddlesden-Popper (RP) phase, which involves the loss of both oxygen anions and cobalt cations upon annealing where the cobalt is found as isolated Co ions or Co nanoparticles. First principles calculations confirm that the concurrent loss of oxygen and cobalt ions is thermodynamically possible through an intermediary BM phase. The strong correlation of the magnetic and electronic properties to the crystal structure highlights the potential of utilizing ion migration as a basis for emerging applications such as neuromorphic computing.

1. Introduction

Ion migration-induced modification of physical properties is an emerging research direction in the search for tunable materials that can revolutionize the growing field of neuromorphic computing.[1-3] Among the candidate materials, perovskite oxides with the chemical formula ABO_3 are of interest because of their wide range of physical properties, high oxygen ion conductivities, and the multitude of related phases such as the Grenier ($ABO_{2.7}$), brownmillerite (BM, $ABO_{2.5}$), square planar (SP, ABO_2),[4,5] and Ruddlesden-Popper ($A_{n+1}B_nO_{3n+1}$ where n = integer)[6,7] phases. Previous studies on these materials have focused on the impact of the A and B stoichiometry,[8,9] however recent studies have turned to the oxygen stoichiometry where topotactic transformations can occur between related structural phases due to a loss or gain of oxygen ions while retaining a relationship in the crystallographic orientation.[10-12] Relative to the parent perovskite phase, oxygen deficiency, δ (where $0 < \delta < 1$), is accommodated by a lowering of the average B-ion valence state and a change in the local coordination environment from corner-shared BO_6 octahedra in the perovskite phase, to alternating layers of BO_6 octahedra and BO_4 tetrahedra in the BM phase (see structural diagrams in **Figure 1(k and m)**). Further reduction from the BM phase can lead to an in-plane BO_4 coordination in the SP phase, or even one of the Ruddlesden-Popper phases, where both B and oxygen ions are partially depleted from the parent perovskite phase. As a result, these structural changes lead to substantial modification to the physical properties.

A gradual progression between the perovskite and BM phases have previously been demonstrated in several complex oxide systems, including $La_{0.7}Sr_{0.3}CoO_3$,[13,14] $La_{0.67}Sr_{0.33}MnO_3$,[15] and $YBa_2Cu_3O_{7-\delta}$,[16] by the deposition of ultrathin Gd layers of varying thickness. The Gd getter layer experienced a spontaneous redox reaction to form GdO_x, leaching oxygen ions from the underlying complex oxide thin films and resulting in a topotactic transformation, which then leads to a change in the magnetic and electrical properties in these complex oxides. Other studies focused on the $SrFeO_{3-\delta}$ and $SrCoO_{3-\delta}$ systems where a reversible transformation between the stable BM $SrFeO_{2.5}$ ($SrCoO_{2.5}$) phase and the metastable $SrFeO_3$ ($SrCoO_3$) perovskite phase was observed with an applied electrical field or under optimized *oxidizing* annealing conditions.[17-22] With further *reduction*, BM $SrFeO_{2.5}$ films could transform to infinite-layer $SrFeO_2$ SP phase.[21,23] However, in the cobaltite system, further *reduction* of BM $SrCoO_{2.5}$ films led to amorphous films or nano-twinned, tetrahedrally-coordinated phases[22,24] rather than the formation of $SrCoO_2$ SP phase or even the Sr_2CoO_4[25,26] Ruddlesden-Popper phase. Therefore, this work investigates the mechanisms and the phase stability associated with cobaltite topotactic transformations.

A series of topotactic transformations were initiated in Sr-doped lanthanum cobaltite ($La_{0.7}Sr_{0.3}CoO_{3-\delta}$, LSCO) thin films exposed to anneals under highly reducing conditions. At this Sr-doping level, the perovskite phase is the equilibrium phase, characterized by coincident metal (M)-to-insulator (I) and ferromagnetic (FM)-to-paramagnetic transitions at the Curie temperature, T_C~240 K,[27] a high oxygen vacancy conductivity, and relatively low oxygen vacancy formation energy.[28] The anneals were performed using either a Mg-trap annealing system[29] or a gas evolution system[30] which enabled the exploration of wide temperature/pressure phase space ranging from room temperature to 1000 °C and oxygen partial pressures from 10^{-25} to 10^{-1} atm (see **Figure 1(a)**). X-ray absorption (XA) spectroscopy, and scanning transmission electron microscopy (STEM) showed that these structural transformations involved a change of the Co local coordination from a mixture of Co^{3+}/Co^{4+} ions in octahedral coordination in the perovskite phase to Co^{2+} ions in octahedral coordination in a $La_{1.4}Sr_{0.6}Co_{1+\upsilon}O_{4-\delta}$ Ruddlesden-Popper (RP) phase (where $0 \leq \upsilon < 1$ and $0 < \delta < 1$) formed under the most reducing conditions. Raman spectroscopy and first principles calculations suggest that the formation of the RP phase involves the loss of both oxygen anions and Co ions through an intermediary BM phase. As a result, the magnetic properties evolved between various FM and antiferromagnetic (AFM) phases, and the room temperature resistivity spanned eight orders of magnitude. Compared to the perovskite and BM phases widely reported in the previous literature, we successfully observed the formation of the RP phase with its own distinct physical

and functional properties. Furthermore, the combination of experiment and theory enabled us to elucidate the formation mechanisms for each of the reduced phases.

2. Experimental and Theoretical Methods

Epitaxial LSCO thin films (thickness of 16~28 nm) were deposited on (001)-oriented LSAT substrates by pulsed laser deposition with a laser pulse frequency of 1 Hz and laser fluence of ~ 0.8 J cm^{-2}. During the growth, the substrate temperature was held at 700 ºC and the oxygen pressure was 300 mTorr. The films were cooled slowly to room temperature after the deposition with an oxygen pressure of 300 Torr to ensure proper oxygen stoichiometry. The LSCO films were annealed for 1 hour either in a gas evolution system which consists of a tube furnace connected to a high vacuum system capable of achieving oxygen partial pressures from 10^{-12} to 0.1 atm and temperatures up to 1000 ºC,[30] or a Mg-based oxygen trap system capable of achieving oxygen partial pressures down to 10^{-25} atm and temperatures up to 400 ºC.[29] In the gas evolution system, the base pressure was maintained at ~10^{-10} atm, and high-purity oxygen (>99.99%) of different pressures ranging from 10^{-12} to 10^{-7} atm was introduced into the annealing chamber using the computer-controlled metal-seated valve.[30] During the Mg-trap annealing experiments, the Mg-based oxygen trap and annealing chamber was maintained at 1 atm total pressure, and the low oxygen partial pressure was generated by flowing ultrahigh purity argon gas through a heated Mg powder bed. The trace amount of oxygen in ultrahigh purity argon reacts with Mg, creating further reduction in the oxygen partial pressure as it flows into the chamber.[29] All of the pressures quoted in the following sections are referring to the oxygen partial pressures, P_{O_2}.

The structural properties of the films were characterized by x-ray reflectivity (XRR) and high-resolution x-ray diffraction (XRD) using either a Bruker D8 Discover or Rigaku Smartlab four-circle diffractometer using Cu $K_{\alpha 1}$ x-rays (8.04 keV). The XRD data for the AG-P LSCO sample was obtained at Beamline 7-2 at the Stanford Synchrotron Radiation Light Source using an x-ray energy of 14 keV. The XRR curves were fit using GenX software to determine the thickness, roughness, and density of the films.[31] A Lakeshore cryogenic probe station was used to measure the film resistivity upon warming from 80 K with the van der Pauw geometry. The bulk magnetic properties were measured using a Quantum Design VersaLab or Physical Property Measurement System vibrating-sample magnetometer (VSM) with the magnetic field applied along the in-plane [100] substrate direction. Soft x-ray magnetic spectroscopy at the Co *L*-edge was performed at 80 K at beamlines 4.0.2 and 6.3.1 at the Advanced Light Source (ALS) using total electron yield detection (TEY, which provides surface sensitive measurements to the top 5-10 nm of the sample), and luminescence yield

detection (LY, which probes the full film thickness[32]). The x-rays were incident upon the sample at a 30° grazing angle along the in-plane [100] substrate direction. X-ray magnetic circular dichroism (XMCD) spectra were calculated as the difference between XA spectra acquired using right/left circularly polarized x-rays with a 1.93 T magnetic field oriented parallel to the propagation direction of the circularly polarized x-rays. X-ray linear dichroism (XLD) spectra were calculated as the difference between XA spectra acquired using *s*- and *p*-polarized x-rays such that the x-ray ***E***-vector is respectively parallel to the in-plane [010] substrate direction or 30° away from the [001] substrate direction, due to the grazing-incidence geometry of the measurements.

High angle annular dark field (HAADF) STEM images and electron energy loss spectroscopy (EELS) mappings were acquired by a double corrector JEOL ARM 300F TEM. A 30 μm condenser aperture was selected for EELS acquisition. The convergent and collection semi-angles are 21 μm and 90 μm, respectively. The samples used for TEM characterizations were made by standard focus ion beam (FEI Helios NanoLab) lift-out method. Raman spectra were measured at room temperature using a Horiba Jobin Yvon T64000 Raman spectrometer. The excitation light of 488 nm was focused onto the sample using a 100x objective. The signal was collected in a backscattering geometry and excitation light was blocked by a notch filter. Photoluminescence (PL) spectra were taken using a home-built system coupling an inverted microscope to an imaging spectrometer. The sample was excited with 405 nm light under a 20x objective. Excitation light was rejected by a long pass filter.

First principles calculations were performed using the Quantum Espresso code (v6.4.1),[33,34] which solves the Kohn-Sham equations of DFT using plane waves and pseudopotentials. In particular we used DFT+U (U = 3 eV as justified in previous calculations),[35] with the PBE generalized gradient approximation[36] for the exchange-correlation functional and the projected augmented wave pseudopotentials from the PSlibrary[37] (v1.0.0 for La, Sr and O, and v0.3.1 for Co). A previously optimized BM structure[35] was used to calculate the formation energy of Co or O vacancies in the BM phase, which was modeled with a 36-atom orthorhombic cell with the stoichiometry of $La_{0.63}Sr_{0.37}CoO_{2.5}$. The initial RP phase was constructed from the La_2CoO_4 structure (ID: mp-27494) from the Materials Project,[38] where we substituted 37.5% La by Sr in this 28-atom orthorhombic cell. Defective BM structures and the RP structure were then optimized within the orthorhombic lattice symmetry, using a plane-wave cutoff of 1224 eV and a Monkhorst-Pack k-point grid[39] with the resolution between 0.02-0.03 $Å^{-1}$. The convergence thresholds for energy, force and pressure were set to 2.0×10^{-4} eV per formula unit (f.u.), 0.02 eV $Å^{-1}$ per f.u. and 0.5 Kbar, respectively.

3. Results and Discussion

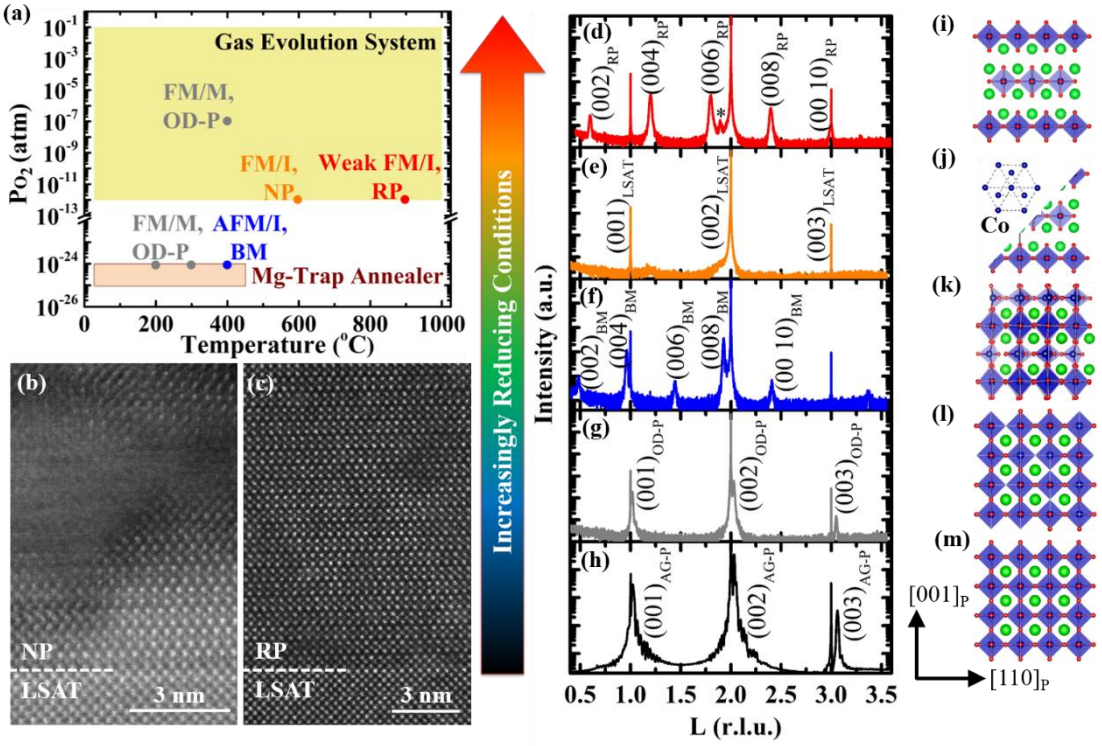

Figure 1. (a) Phase diagram of the structural, magnetic, and electrical properties of LSCO films exposed to anneals under highly reducing conditions. (b-c) HAADF STEM images of the NP and RP samples, respectively. (d-h) XRD curves, and (i-m) crystal structure diagrams for the annealed LSCO films. The XRD curves show sharp, high intensity peaks arising from the LSAT substrate and weaker film peaks arising from the (00*L*) planes of the respective structure. In (d), the * peak results from the sample holder. In (i-m), the green and red atoms represent La/Sr and oxygen ions, respectively, while Co ions (blue) sit in the center of the octahedra/tetrahedra. As shown in (j), this NP phase consisted of both the polycrystalline grains of the RP phase. The metallic Co nanoparticles are not observed due to their small size, low density, and/or their misalignment relative to the zone axis of the image.

The range of possible annealing conditions available with the gas evolution and Mg-trap annealing systems is indicated by the shaded regions in **Figure 1(a),** while the symbols represent the conditions explored in this work. Upon exposure to increasingly reducing conditions (*i.e.*, lower oxygen partial pressure and/or higher temperature), the LSCO thin films gradually underwent several topotactic transformations as revealed through XRR (**Figure S1**) and XRD measurements (**Figure 1(d)-(h)**). The XRR curves reveal substantial changes in the film thickness, density, and roughness associated with each of these transformations. **Table S1** and **S2** list the parameters obtained from fitting the

XRR curves using GenX software.[31] For anneals up to 600 °C/10^{-12} atm P_{O_2}, a trend of decreasing density and increasing film thickness and roughness can be observed, as expected for perovskite-related materials with increasing oxygen deficiency.[40,41] In particular, the LSCO thin film annealed at 600 °C/10^{-12} atm P_{O_2}, experiences a 50.5% increase in the total film thickness (18.6 nm to 28.0 nm) and 29.9% decrease in the main layer density (6.79 g cm^{-3} to 4.76 g cm^{-3}). Finally, increasing the annealing temperature to 900 °C/10^{-12} atm P_{O_2} leads to a recovery of the film density to 6.28 g cm^{-3} (22.6% decrease from the as-grown perovskite (AG-P) sample) and roughness, accompanied with a small decrease in thickness to 17.3 nm (5.46% decrease). Therefore, the XRR results suggest that these highly reduced films have experienced substantial structural modification upon annealing.

Analysis of ω-2θ XRD curves (**Figure 1(d)-(h)**) enable the identification of the phases present after each reducing anneal. Reciprocal space maps (RSMs, **Figure S2**) show that the thin films remain coherently strained to the underlying $(LaAlO_3)_{0.3}(Sr_2TaAlO_6)_{0.7}$ (LSAT) substrate regardless of annealing conditions. **Figure 1(h)** shows the expected series of (00*L*) peaks for the perovskite phase with an out-of-plane lattice parameter of 3.806 Å. Upon annealing at 200 °C and 300 °C/10^{-24} atm P_{O_2}, as well as 400 °C/10^{-7} atm P_{O_2}, the same series of (00*L*) peaks can be observed (**Figure 1(g)**), indicating that the perovskite phase is maintained. However, the film peaks are shifted to slightly lower 2θ values compared to the AG-P phase. For the sample annealed 400 °C/10^{-7} atm P_{O_2}, the out-of-plane lattice parameter increases slightly to 3.812 Å which is consistent with the 6.0% decrease in density obtained from the XRR curves, and consistent with an oxygen deficient perovskite (OD-P) phase.[42,43]

Annealing the LSCO thin films at 400 °C/10^{-24} atm P_{O_2} resulted in the transformation to the BM phase, as characterized by the dramatic shift of the main (00*L*) film peaks to the low angle side of the LSAT substrate peak, as well as the appearance of prominent half-order peaks due to the quadrupling of the unit cell from the alternating octahedral and tetrahedral layers. The lattice parameter for this BM phase is 16.053 Å. The XRR curves indicate a 6.7% increase in total film thickness and 13% decrease in density accompany the transformation to the BM phase, consistent with prior studies of the perovskite-BM transformation in $SrCoO_{3-\delta}$[1,10,17] and $La_{0.7}Sr_{0.3}CoO_{3-\delta}$[13] films. The BM $La_{0.7}Sr_{0.3}CoO_{2.5}$ phase was found to be metastable and slowly transformed back to the perovskite phase over a period of several months at room temperature in air, even when capped with 5 nm Gd/5 nm Au to try to prevent oxygen reincorporation into the film.

Upon annealing at 600 $^{o}C/10^{-12}$ atm P_{O_2}, the film peaks disappear as shown in **Figure 1(e)**. This absence of film peaks could be explained by amorphization of the LSCO thin film or the formation of a nano-textured phase where the film breaks up into small crystalline regions in which the planes are not oriented parallel to the substrate surface. HAADF STEM images (**Figure 1(b)**) demonstrated that after annealing, this sample consisted primarily of polycrystalline grains of the RP phase separated by amorphous regions/regions of low crystallinity, or regions misaligned to the zone axis of the image. The out-of-plane lattice parameter of this polycrystalline RP structure is 12.25 ± 0.21 Å, where the (001) planes are not perfectly aligned with the underlying LSAT substrate due to the presence of defects and dislocations at the film-substrate interface. Furthermore, EELS elemental mapping in **Figure 2** demonstrates that this thin film has a non-uniform Co distribution while maintaining more uniform distributions of the La and O ions. In **Figure 2(e)**, the Raman spectra showed peaks at 683, 1366, and 1590 cm^{-1}, which can be assigned to the Raman lines of Co nanoparticles.[44-46] Therefore, we refer to this sample as the nanoparticle (NP) sample. The formation of the Co nanoparticles accounts for the loss of Co ions needed in order to form the RP phase, however their small size, low density, and/or random orientation precludes their observation in XRD or STEM measurements. Similar effects have been observed in the electrodes of solid oxide fuel cells where nickel particles exsolved from nickel oxides.[47,48] Due to their small size, the Co nanoparticles are not observed in the XRD curves or STEM images.

As the LSCO thin films were annealed at 900 $^{o}C/10^{-12}$ atm P_{O_2}, a new epitaxial phase emerged with a pattern of peaks distinct from the perovskite or BM phases. These peaks can be indexed to an out-of-plane lattice parameter of 12.89 Å. A lack of thickness fringes (**Figure S3**) indicates that compared to the AG-P sample, this phase has large interfacial roughness and d-spacing variations, further confirmed by XRR in **Figure S1** and **Table S2**. HAADF STEM imaging (**Figure 1(c)**) confirmed that this sample consists of a single crystalline $La_{1.4}Sr_{0.6}Co_{1+\upsilon}O_{4-\delta}$ RP structure[7] with an out-of-plane lattice parameter of 12.83 ± 0.05 Å which is coherently strained to the underlying LSAT substrate. Raman spectra showed that the Co nanoparticles were no longer present, however, PL spectra (**Figure 2(f)**) show multi-peaked emission spanning the visible and near-infrared wavelengths (from 480 to 755 nm). Similar spectra have been observed from isolated Co^{2+} ions in a variety of host crystals,[49-51] suggesting that these PL features also arise from excess Co ions that are generated when the LSCO thin films are reduced. Unlike the BM phase, this RP phase is stable under ambient conditions for a timeframe of years, as determined through XRD measurements.

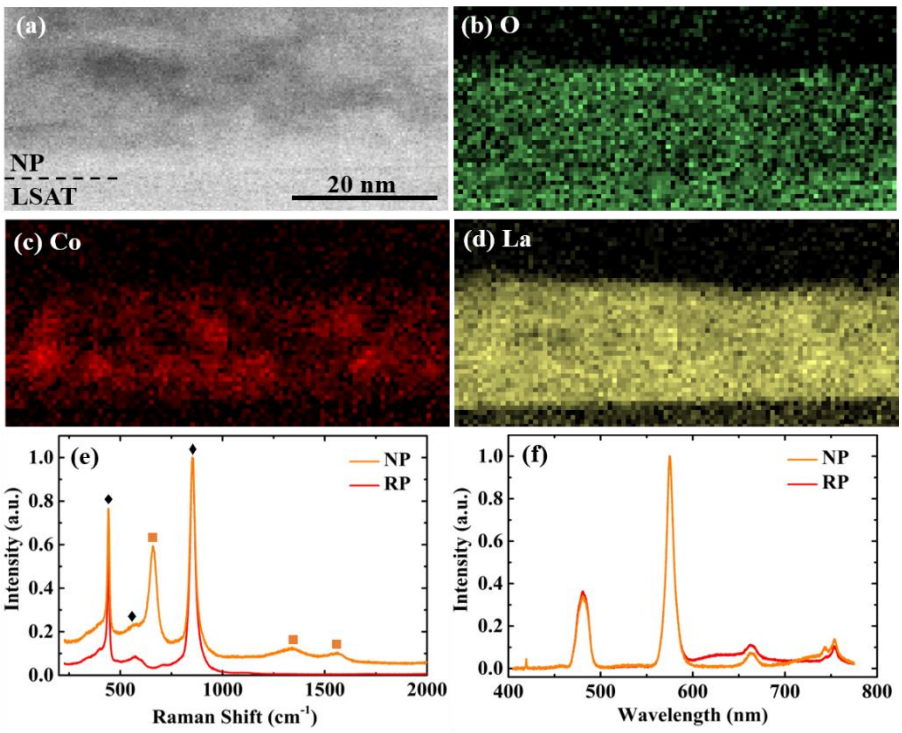

Figure 2. (a) EELS elemental mapping of the NP sample taken at the substrate-film interface showing maps of the (b) oxygen, (c) cobalt, and (d) lanthanum edges. (e) Raman and (f) PL spectra of the NP (orange) and RP (red) samples. Raman lines from the LSAT substrate[52] are denoted with the black diamond symbols (♦), while those from the cobalt nanoparticles are denoted with the orange squares (■). In (f), all of the PL features arise from the excess Co ions in the NP and RP films.

Density functional theory (DFT) calculations further support the assignment of the RP phase to the 900 °C annealed sample, as the calculated structural, magnetic and electronic properties (**Table S3**) all showed good agreement with experimental measurements. In particular, the computed out-of-plane lattice parameter decreased by 19.5 % in the transformation from the BM phase (15.86 Å) to the RP phase (12.76 Å), consistent with the experimentally observed 20% change from BM (16.053 Å) to the 900 °C annealed sample (12.83 Å). A G-type AFM ordering with insulating properties was identified in the calculations with a small net magnetic moment ~0.25 μ_B per Co ion, consistent with the high resistivity and weak FM properties identified below 25 K (as further discussed below). Moreover, our calculated formation energy of cobalt and oxygen vacancies in the BM phase (see **Table S4** and the related discussion) revealed that the BM to RP phase transition is thermodynamically possible; indeed we found that the cobalt vacancy requires lower energy to form than the oxygen vacancy in the BM phase, either at the standard condition (27 ^{o}C/1 atm) or at the 600 ^{o}C/10^{-12} atm P_{O_2} annealing condition, and their formation energies are comparable at the 900 ^{o}C/10^{-12}

atm P_{O_2} annealing condition. This result indicates that the loss of cobalt and oxygen ions in the BM phase is likely, which is a necessary step to form the RP phase and justifies the appearance of Co nanoparticles detected in experiments.

XA spectra (**Figure 3(a) and S4**) were acquired in order to detect the change in Co valence state and local coordination associated with the topotactic transformations. Reference spectra for Co^{2+} ions in octahedral coordination ($CoFe_2O_4$[53]) and metallic Co are included for comparison. The AG-P sample agrees with literature data for mixed valence Co^{3+}/Co^{4+} ion in octahedral coordination.[54,55] The OD-P sample shows only subtle changes compared the AG-P sample in the form of slightly less defined spectral features. On the other hand, the XA spectra of the highly reduced phases (BM, NP, and RP) show clear signatures of Co^{2+} ions in octahedral coordination with subtle differences in the intensities of the three main spectral features denoted with (A)-(C) dotted lines. The decrease in the Co valence state in the highly reduced phases is expected in order to maintain charge neutrality upon increase in oxygen deficiency, δ. The subtle spectral differences for the highly reduced phases likely arise from the fact that the Co ions in the BM sample are in mixed octahedral/tetrahedral coordination, while those in the NP and RP samples also have contributions from the Co nanoparticles and isolated Co ions, respectively. In the ideal RP structure with the chemical formula of $La_{1.4}Sr_{0.6}CoO_4$, the average Co valence state is $Co^{2.6+}$; however, our annealed NP and RP samples are likely Co-rich with stoichiometry of $La_{1.4}Sr_{0.6}Co_{1+\upsilon}O_{4-\delta}$, where $0 \leq \upsilon < 1$, resulting in lower average Co valence state.

XMCD measurements at the Co $L_{3,2}$ absorption edges (**Figure 3(b)**) provide complementary information on the element/coordination specific contributions to the FM properties of the annealed LSCO thin films. Compared to the AG-P sample, the saturation magnetization (M_S) of the OD-P films decreased by 60% as the oxygen vacancies break up the Co^{3+} - O^{2-} - Co^{4+} double exchange network[56,57] and potentially introduces local AFM structures for Co ions near vacancies.[35,58] While the XA spectra for the BM, NP, and RP samples were similar (**Figure 3(a)**), stark differences exist in the XMCD spectra. No FM signal was detected for the RP sample at 80 K, and the BM sample showed a weak FM signal with spectral features matching that of Co^{2+} ions in octahedral coordination. The XMCD magnitude of the BM sample is only 4.7% of the $CoFe_2O_4$ reference spectra. In contrast, the sample referred to as the NP phase shows a broad negative peak without the multiplet structure typically found in complex oxides and is more reminiscent of metallic Co atoms. Fitting of the XA and XMCD spectra for this sample (**Figure S5**) shows that it can be considered as a mixture consisting of ~ 77% of RP phase and ~ 23% metallic Co, consistent with the Raman spectra. As

shown in **Figure S6**, the hysteresis loops show that this phase has a substantially lower coercivity compared to the AG-P phase (*i.e.*, H_C = 0.1 T compared to H_C ~ 1.25 T, respectively), consistent with Co nanoparticles.[59,60]

The bulk magnetic and electrical properties of the annealed LSCO thin films are shown in **Figure 4**. The resistivity data was normalized to the thin film volume, while the magnetization data was normalized to 1. In the resistivity measurement, the transition temperature was determined as the temperature where the curve has a local maximum (*i.e.* dR/dT=0),[61,62] while the Curie temperature was determined as the temperature corresponding to the peak in $|dM/dT|$.[63] Using these metrics, the transition temperatures are in good agreement between the two measurements. For the AG-P sample, the M-to-I and FM-to-PM transitions coincide at T_C~198 K. The oxygen deficiency in the OD-P phase led to a decrease in T_C to 180 K and an increase in resistivity across the entire temperature range studied. The increase in resistivity is most dramatic at low temperatures where an additional insulating phase emerges for temperatures below ~125 K.[64,65] The highly reduced phases (BM, NP, and RP) had room temperature resistivity values several orders of magnitude higher than the perovskite phases. The high resistivity values for the NP and RP phases prevented resistivity measurements at lower temperatures. The BM phase displayed purely insulating temperature dependence and no detectable magnetic signal over the temperature range studied, consistent with the AFM properties reported for BM $SrCoO_{2.5}$.[66] XLD measurements suggest that these AFM properties also remain in the $La_{0.7}Sr_{0.3}CoO_{2.5}$ phase studied here (**Figure S7**). The weak FM signal from the BM phase measured in the XMCD spectrum (**Figure 3(b)** blue curve) was not detected in the magnetization-temperature plot in **Figure 4(b),** mainly due to the detection sensitivity difference between the two measurements. In addition to the insulating properties, the NP phase displayed FM properties with a nearly constant magnetization value of 847 emu cm^{-3} up to the highest measurement temperature of 370 K. This magnetization value was normalized to the estimated volume of all the Co nanoparticles (*i.e.*, 23% of the total NP film volume, based on XA spectra fitting results), and the measured M_S of these Co nanoparticles corresponds well to the reported value for metallic Co (*i.e.*, M_S = 1352 emu cm^{-3} compared to M_S ~1400 emu cm^{-3},[67,68] respectively). The high T_C value in the NP sample is also consistent with the presence of FM Co nanoparticles embedded within an insulating matrix. The RP phase has a weak FM phase with low remanent magnetization which appears at temperatures below ~25 K (not shown).

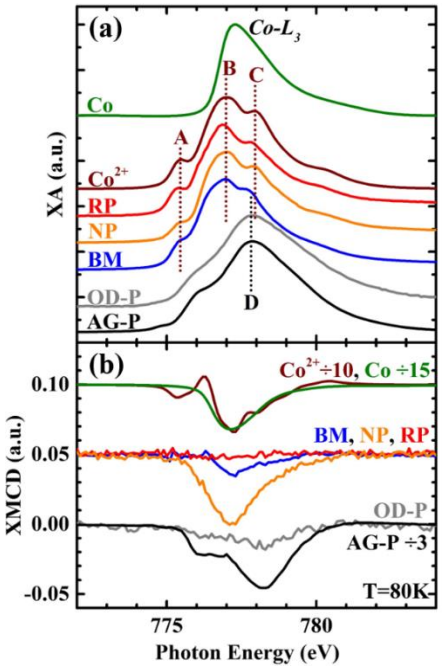

Figure 3. (a) Co $L_{3,2}$ XA and (b) XMCD spectra acquired at 80 K for LSCO thin films after reducing anneals. Reference spectra for Co^{2+} ions in octahedral coordination[53] and metallic Co are also included. The XA spectral features of Co^{2+} ions are denoted with (A-C) dotted lines and the main peak of the Co^{3+}/Co^{4+} ions with a (D) dotted line.

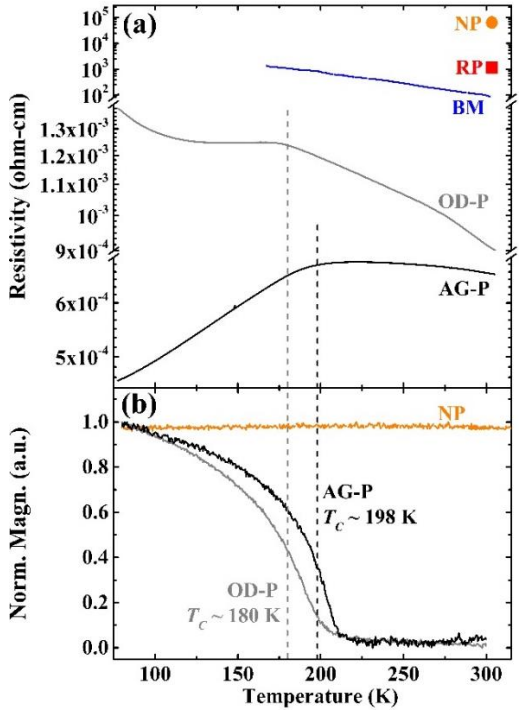

Figure 4. Film-averaged (a) resistivity and (b) normalized magnetization as a function of temperature for LSCO thin films after reducing anneals. A magnetic field of 0.08 T was applied along the [100] substrate direction during the magnetization measurements.

Figure 1(a) summarizes the temperature/oxygen partial pressure phase space explored in order to initiate a wide range of topotactic transformations in perovskite LSCO thin films. Under mild reducing conditions ($T \leq 300$°C at 10^{-24} atm P_{O_2}, and 400°C at 10^{-7} atm P_{O_2}), oxygen deficiency resulted in a slight expansion of the perovskite unit cell volume, a change in the magnetic properties (decrease in T_C and M_S), and an increase in the resistivity due to the disruption of the Co^{3+} - O^{2-} - Co^{4+} double exchange network. Increasing the annealing temperature to 400 °C at 10^{-24} atm P_{O_2}, resulted in the formation of the BM phase, which displayed AFM/I properties with a trace FM signal from Co^{2+} ions. This metastable phase slowly transformed back to the perovskite phase over a period of several months in ambient conditions. Annealing at 600 °C/10^{-12} atm P_{O_2} led to the formation of small Co nanoparticles embedded in a polycrystalline matrix of the RP phase characterized by FM/I properties by low coercivity and an elevated Curie temperature, $T_C > 370$ K. Notably, this structure was characterized by a dramatic increase in total film thickness (50.5%) and a sharp drop in density (-29.9%) compared to the AG-P thin film. Finally, an epitaxial RP structure ($a = b = 3.868$ Å, $c = 12.89$ Å) was obtained after annealing at the most reducing condition explored (900 °C/10^{-12} atm P_{O_2}). Once formed, this phase remained stable under ambient conditions, and it displayed high resistivity and weak FM properties at temperatures below ~ 25 K with low remanent magnetization.

4. Conclusions

In summary, a series of topotactic transformations involving the loss of both oxygen anions and cobalt cations were observed in $La_{0.7}Sr_{0.3}CoO_{3-\delta}$ thin films upon annealing under highly reducing conditions. First principles calculations were conducted to interpret experiments and characterize the observed phases. These phases not only include the oxygen-deficient perovskite and BM phases, but the RP phase which has been rarely reported in the cobaltite topotactic transformations and requires the loss of cobalt cations. A composite phase consisting of FM Co nanoparticles embedded in an insulating RP matrix was observed at an intermediate annealing condition of 600 °C/10^{-12} atm P_{O_2}. These Co nanoparticle precipitates re-dissolved into the oxide matrix upon annealing, forming interstitial Co ions in the RP phase under the most reducing condition investigated. DFT calculations further confirmed that the formation of the RP phase and Co nanoparticles is thermodynamically possible, and the calculated structural, magnetic and electronic properties supported the experimental measurements. Each structure possessed its own distinct set of physical properties including FM/M, AFM/I, and two types of FM/I phases. The ability to control the physical properties by movement of ion migration suggest their potential for further exploration into the reversibility and order parameter tuning by electric fields for

applications such as neuromorphic devices.

Acknowledgements

This work was supported as part of the Quantum Materials for Energy Efficient Neuromorphic Computing, an Energy Frontier Research Center funded by the U.S. Department of Energy, Office of Science, Basic Energy Sciences under Award DE-SC0019273. The Mg-trap annealing experiments were conducted by Z. Zhang supported by AFOSR FA9550-18-1-0250 and the gas evolution system was developed under award number FA9550-20-1-0242. This research used resources of the Advanced Light Source, which is a DOE Office of Science User Facility under Contract No. DE-AC02-05CH1123. Use of the Stanford Synchrotron Radiation Light Source, SLAC National Accelerator Laboratory, is supported by the US Department of Energy, Office of Science, Office of Basic Energy Sciences under Contract No. DE-AC02-76SF00515. The authors acknowledge the use of the Nanostructures Cleanroom Facility within the California NanoSystems Institute, supported by the University of California, Santa Barbara and the University of California, Office of the President.

References

[1] Q. Lu and B. Yildiz, Nano Letters **16**, 1186 (2016).

[2] C. Eames, J. M. Frost, P. R. F. Barnes, B. C. O'Regan, A. Walsh, and M. S. Islam, Nature Communications **6**, 7497 (2015).

[3] H.-T. Zhang, Z. Zhang, H. Zhou, H. Tanaka, D. D. Fong, and S. Ramanathan, Advances in Physics: X **4**, 1523686 (2019).

[4] M. T. Anderson, J. T. Vaughey, and K. R. Poeppelmeier, Chem. Mater. **5**, 151 (1993).

[5] T. G. Parsons, H. D'Hondt, J. Hadermann, and M. A. Hayward, Chem. Mater. **21**, 5527 (2009).

[6] M. A. Zurbuchen *et al.*, Journal of Materials Research **22**, 1439 (2007).

[7] J. Li *et al.*, Nano Energy **78**, 105215 (2020).

[8] W. Jian, R. Jia, H.-X. Zhang, and F.-Q. Bai, Inorganic Chemistry Frontiers (2020).

[9] S. Tan, F. Sayed, S. Yang, Z. Li, J. Wu, and P. M. Ajayan, ACS Materials Letters **1**, 230 (2019).

[10] H. Jeen, W. S. Choi, J. W. Freeland, H. Ohta, C. U. Jung, and H. N. Lee, Advanced Materials **25**, 3651 (2013).

[11] H. Jeen *et al.*, Nature Materials **12**, 1057 (2013).

[12] J. Walter, H. Wang, B. Luo, C. D. Frisbie, and C. Leighton, ACS Nano **10**, 7799 (2016).

[13] D. A. Gilbert *et al.*, Physical Review Materials **2**, 104402 (2018).
[14] G. Rippy *et al.*, Physical Review Materials **3**, 082001 (2019).
[15] A. J. Grutter, D. A. Gilbert, U. S. Alaan, E. Arenholz, B. B. Maranville, J. A. Borchers, Y. Suzuki, K. Liu, and B. J. Kirby, Applied Physics Letters **108**, 082405 (2016).
[16] P. D. Murray *et al.*, ACS Applied Materials & Interfaces **12**, 4741 (2020).
[17] H. Jeen *et al.*, Nature Materials **12**, 1057 (2013).
[18] Q. Lu and B. Yildiz, Nano Letters **16**, 1186 (2016).
[19] N. Lu *et al.*, Nature **546**, 124 (2017).
[20] V. R. Nallagatla *et al.*, Advanced Materials **31**, 1903391 (2019).
[21] C. Tassel and H. Kageyama, Chemical Society Reviews **41**, 2025 (2012).
[22] N. Ichikawa, M. Iwanowska, M. Kawai, C. Calers, W. Paulus, and Y. Shimakawa, Dalton Transactions **41**, 10507 (2012).
[23] Y. Tsujimoto *et al.*, Nature **450**, 1062 (2007).
[24] Q. Zhang *et al.*, Nature Communications **8**, 104 (2017).
[25] S. K. Pandey, Physical Review B **81**, 035114 (2010).
[26] Q. Li, X. Yuan, L. Xing, and M. Xu, Scientific Reports **6**, 27712 (2016).
[27] J. Wu, J. W. Lynn, C. J. Glinka, J. Burley, H. Zheng, J. F. Mitchell, and C. Leighton, Phys. Rev. Lett. **94**, 037201 (2005).
[28] T. Ishihara, *Perovskite Oxide for Solid Oxide Fuel Cells* (Springer, 2009).
[29] Z. Zhang *et al.*, Physical Review Applied **7**, 034008 (2017).
[30] M.-H. Lee, Y. Kalcheim, J. d. Valle, and I. K. Schuller, ACS Applied Materials & Interfaces **13**, 887 (2021).
[31] M. Bjorck and G. Andersson, Journal of Applied Crystallography **40**, 1174 (2007).
[32] A. Bianconi, D. Jackson, and K. Monahan, Physical Review B **17**, 2021 (1978).
[33] P. Giannozzi *et al.*, Journal of Physics: Condensed Matter **29**, 465901 (2017).
[34] P. Giannozzi *et al.*, Journal of Physics: Condensed Matter **21**, 395502 (2009).
[35] S. Zhang and G. Galli, npj Computational Materials **6**, 170 (2020).
[36]J. P. Perdew, K. Burke, and M. Ernzerhof, Physical Review Letters **77**, 3865 (1996).
[37] A. Dal Corso, Computational Materials Science **95**, 337 (2014).
[38] A. Jain *et al.*, APL Materials **1**, 011002 (2013).
[39] H. J. Monkhorst and J. D. Pack, Physical Review B **13**, 5188 (1976).
[40] T. Ishihara, in *Springer Handbook of Electronic and Photonic Materials*, edited by S. Kasap, and P. Capper (Springer International Publishing, Cham, 2017), pp. 1.
[41] X. Liu *et al.*, Advanced Science **6**, 1801898 (2019).
[42] Y. Chen, D. D. Fong, F. W. Herbert, J. Rault, J.-P. Rueff, N. Tsvetkov, and B. Yildiz, Chemistry of Materials **30**, 3359 (2018).
[43] Chen, Yu, and S. B. Adler, Chemistry of Materials **17**, 4537 (2005).

[44] S. M. Ansari, R. D. Bhor, K. R. Pai, D. Sen, S. Mazumder, K. Ghosh, Y. D. Kolekar, and C. V. Ramana, Applied Surface Science **414**, 171 (2017).
[45] H. Yoon, A. Xu, G. E. Sterbinsky, D. A. Arena, Z. Wang, P. W. Stephens, Y. S. Meng, and K. J. Carroll, Physical Chemistry Chemical Physics **17**, 1070 (2015).
[46] E. Rauwel, S. Al-Arag, H. Salehi, C. O. Amorim, F. Cuisinier, M. Guha, M. S. Rosario, and P. Rauwel, International journal of nanomedicine **15**, 7051 (2020).
[47] M. Bahout, P. B. Managutti, V. Dorcet, A. Le Gal La Salle, S. Paofai, and T. C. Hansen, Journal of Materials Chemistry A **8**, 3590 (2020).
[48] G. Yang, W. Zhou, M. Liu, and Z. Shao, ACS Applied Materials & Interfaces **8**, 35308 (2016).
[49] N. V. Kuleshov, V. P. Mikhailov, V. G. Scherbitsky, P. V. Prokoshin, and K. V. Yumashev, Journal of Luminescence **55**, 265 (1993).
[50] K. Ravindranadh, B. Babu, M. C. Rao, J. Shim, C. Venkata Reddy, and R. V. S. S. N. Ravikumar, Journal of Materials Science: Materials in Electronics **26**, 6667 (2015).
[51] N. Sabir, W. Qayyum, S. Z. Hussain, I. Hussain, and F. Amin, *Photoluminescence properties of Co and Ni co-doped CdS/ZnS core/shell nanoparticles* (SPIE, 2018), Vol. 10507, SPIE BiOS, p.^pp. PWB.
[52] T. N. Nunley, T. I. Willett-Gies, J. A. Cooke, F. S. Manciu, P. Marsik, C. Bernhard, and S. Zollner, Journal of Vacuum Science & Technology A **34**, 051507 (2016).
[53] R. V. Chopdekar *et al.*, Journal of Magnetism and Magnetic Materials **322**, 2915 (2010).
[54] A. M. Kane, I. T. Chiu, N. J. Ahlm, R. V. Chopdekar, A. T. N'Diaye, E. Arenholz, A. Mehta, V. Lauter, and Y. Takamura, ACS Applied Materials & Interfaces **12**, 45437 (2020).
[55] M. Merz *et al.*, Physical Review B **82**, 174416 (2010).
[56] B. Bechlars, D. M. D'Alessandro, D. M. Jenkins, A. T. Iavarone, S. D. Glover, C. P. Kubiak, and J. R. Long, Nature Chemistry **2**, 362 (2010).
[57] J. H. Lee, W. S. Choi, H. Jeen, H. J. Lee, J. H. Seo, J. Nam, M. S. Yeom, and H. N. Lee, Scientific Reports **7**, 16066 (2017).
[58] N. Biškup, J. Salafranca, V. Mehta, M. P. Oxley, Y. Suzuki, S. J. Pennycook, S. T. Pantelides, and M. Varela, Physical Review Letters **112**, 087202 (2014).
[59] B. Morcos, P. Lecante, R. Morel, P.-H. Haumesser, and C. C. Santini, Langmuir **34**, 7086 (2018).
[60] K. S. Rao, T. Balaji, Y. Lingappaa, M. R. P. Reddy, and T. L. Prakash, Journal of Experimental Nanoscience **8**, 162 (2013).
[61] B. J. Chen *et al.*, Physical Review B **90**, 155202 (2014).
[62] S. K. Bose, J. Kudrnovský, V. Drchal, and I. Turek, Physical Review B **84**, 174422 (2011).

[63] T. Ma *et al.*, Nature Communications **8**, 13937 (2017).
[64] A. Maignan, D. Pelloquin, C. Martin, M. Hervieu, and B. Raveau, Journal of Materials Chemistry **12**, 1009 (2002).
[65] T. Motohashi, V. Caignaert, V. Pralong, M. Hervieu, A. Maignan, and B. Raveau, Applied Physics Letters **86**, 192504 (2005).
[66] A. Munoz, C. de la Calle, J. A. Alonso, P. M. Botta, V. Pardo, D. Baldomir, and J. Rivas, Phys. Rev. B **78**, 054404 (2008).
[67] J. Schwerdt, G. Goya, M. P. Calatayud, C. Herenu, P. Reggiani, and R. Goya, Current gene therapy **12**, 116 (2012).
[68] V. A. Bautin, A. G. Seferyan, M. S. Nesmeyanov, and N. A. Usov, AIP Advances **7**, 045103 (2017).